Macromolecules

Article

Effect of Thermal History and Shear on the Viscoelastic Response of *i*PP Containing an Oxalamide-Based Organic Compound

Carolus H. R. M. Wilsens,*,[†] Laurence G. D. Hawke,*,[†] Gijs W. de Kort,[†] Sarah Saidi,[‡,§] Manta Roy,[†] Nils Leoné,[†] Daniel Hermida-Merino,[§] Gerrit W. M. Peters,[‖] and Sanjay Rastogi[†]

[†]Aachen-Maastricht Institute of BioBased Materials (AMIBM), Maastricht University, P.O. Box 616, 6200MD Maastricht, The Netherlands
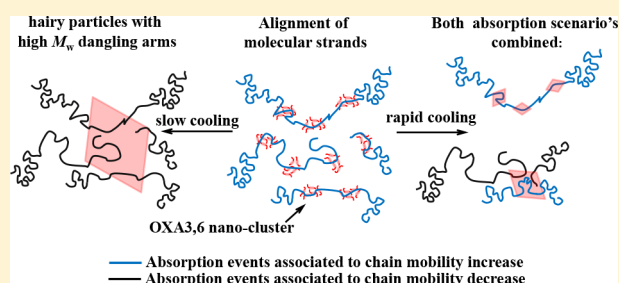
[‡]LMOPS, EA 4423, Université de Lorraine, CentraleSupelec Metz, 2 rue Edouard Belin, F-57070 Metz, France

[§]Netherlands Organisation for Scientific Research (NWO), DUBBLE@ESRF BP CS40220, 38043 Grenoble, France

[‖]Department of Mechanical Engineering, Materials Technology Institute, Eindhoven University of Technology, P.O. Box 513, 5600 MB Eindhoven, The Netherlands

S *Supporting Information*

ABSTRACT: We report on the role of temperature and shear on the melt behavior of *i*PP in the presence of the organic compound N1,N1′-(propane-1,3-diyl)bis(N2-hexyloxalamide) (**OXA3,6**). It is demonstrated that **OXA3,6** facilitates a viscosity suppression when it resides in the molten state. The viscosity suppression is attributed to the interaction of *i*PP chains/subchains with molten **OXA3,6** nanoclusters. The exact molecular mechanism has not been identified; nevertheless, a tentative explanation is proposed. The observed viscosity suppression appears similar to that encountered in polymer melts filled with solid nanoparticles, with the difference that the **OXA3,6** compound reported in this study facilitates the viscosity suppression in the molten state. Upon cooling, as crystal growth of **OXA3,6** progresses, the decrease in viscosity is suppressed. Retrospectively, segmental absorption of *i*PP chains on the surface of micrometer-sized **OXA3,6** crystallites favors the formation of dangling arms, yielding **OXA3,6** crystallites decorated with partially absorbed *i*PP chains. In other words, the resulting **OXA3,6** particle morphology resembles that of a hairy particle or a starlike polymer chain. Such hairy particles effectively facilitate a viscosity enhancement, similar to branched polymer chains. This hypothesis and its implications for the shear behavior of *i*PP are discussed and supported using plate−plate rheometry and slit-flow experiments combined with small-angle X-ray scattering analysis.

INTRODUCTION

Identification and optimization of the nucleation and crystal growth processes in semicrystalline polymers such as isotactic polypropylene (*i*PP) have been investigated over decades.[1] One route to enhance the nucleation process under quiescent conditions is the introduction of (foreign) organic or inorganic components that facilitate heterogeneous nucleation, i.e., the addition of a nucleating agent (NA).[2] Another route involves the application of shear flow which can generate pointlike nuclei that, in turn, can develop into row nuclei by alignment and aggregation until finally a shish is formed.[3,4] The generation of shear-induced precursors lowers the barrier for nucleation and, dependent on the applied shear and time, stimulates crystal growth either perpendicular to the shear direction or in an isotropic fashion.[5−7] The application of shear on polymer melts in the presence of nucleating fillers can enhance the nucleation process even further: Shear enhances the velocity gradient close to the filler, resulting in a local enhancement of the crystallization kinetics.[8] Additionally, in particular for nanoparticle filled systems, adsorption of polymer chains on the particle surface is found to influence the viscoelastic response and thus the shear behavior of the material.[9]

Hydrogen-bonding organic compounds, such as the aliphatic oxalamide N1,N1′-(propane-1,3-diyl)bis(N2-hexyloxalamide) (**OXA3,6**, Figure 1A), have gained quite some attention over the past years due to their ability to suppress the nucleation barrier for various polymers.[10−22] To be an efficient NA, these molecules are designed to (1) dissolve in a polymer matrix during processing and (2) crystallize upon cooling. The dissolution and crystallization process is found to be dependent on the **OXA3,6** concentration, as shown in Figure 1B. Additionally, the nucleating efficiency of the polymer is found to be dependent on the NA particle size, size distribution, shape, and the time given for **OXA3,6** crystallization: Combined, these parameters govern the
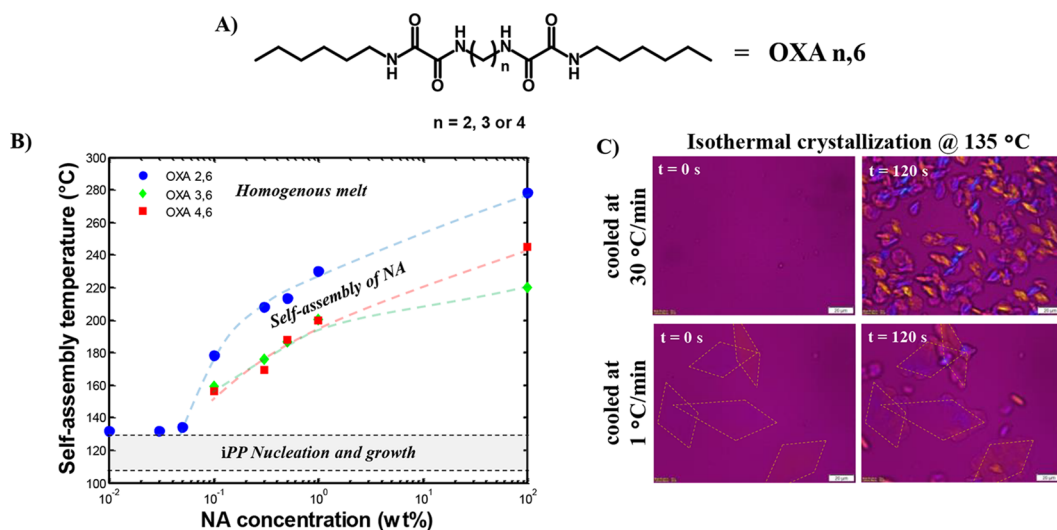
Figure 1. (A) Chemical structure of oxalamide based nucleating agents. (B) Phase diagram showing the self-assembly of **OXA 2,6**, **OXA 3,6**, and **OXA 4,6** in *i*PP during cooling (10 °C/min) as a function of NA concentration. (C) Polarization optical micrographs taken during isothermal crystallization of *i*PP in the presence of 0.5 wt % **OXA3,6**. Prior to isothermal crystallization, the sample was cooled from 200 to 170 °C at a rate of 30 °C/min (top) and 1 °C/min (bottom). After reaching 170 °C, the sample was cooled at a rate of 30 °C/min to 135 °C, after which the crystallization morphology was monitored over time. Because of the poor visibility of the NA particles, yellow dotted lines are placed over borders of the NA aggregates formed during cooling at a rate of 1 °C/min. Images B and C are adapted with permission from refs 10 and 23, respectively.

surface-to-volume ratio of the dispersed nucleating agent. Because the self-assembly of **OXA3,6** proceeds via a nucleation and growth mechanism, the resultant particle morphology is found to be strongly dependent on parameters such as the application of shear, concentration, and cooling rates (Figure 1C).[10,23]

In addition to the nucleating efficiency, recently we reported that **OXA3,6** facilitates a suppression in the apparent viscosity of the polypropylene matrix.[23] With the help of molecular modeling, we established that the viscosity suppression does not originate from differences in molecular weight, topology, or a solvent effect. Instead, we suggested that the suppression in apparent viscosity, in the presence of **OXA3,6**, is similar to that observed in polymeric systems filled with nanoparticles such as carbon nanotubes or graphene or silica.[24−28] High molecular weight *i*PP chains were considered to be physically absorbed on the dispersed nucleating agent surface, thereby effectively withdrawing them from the polymer melt.[29] Because of the effective contribution of the high molar mass component in the structure development, *i*PP was found to be less sensitive to shear in slit flow (i.e., lowered Weissenberg number[30]) in the presence of **OXA3,6**, resulting in the formation of significantly thinner shear layers compared to the pure *i*PP sample.[23] However, despite the suppression in apparent viscosity, systems containing **OXA3,6** exhibited a decrease in the crystallization time and a more homogeneous crystallization morphology. Though these findings are interesting, a clear understanding on the origin and correlation between the viscosity suppression and shear is not available. To address these points, in this study we report on a series of experiments where we identify the effects of **OXA3,6** concentration, thermal history, and shear on the apparent viscosity suppression of *i*PP. For the shear experiments, we make use of a slit-flow device equipped with diamond windows, which allows us to subject the polymer melt to high but well-defined shear rates and to follow the time-resolved structure development using X-ray scattering.

EXPERIMENTAL SECTION

Material Preparation and Blending Process. *N*1,*N*1′-(Propane-1,3-diyl)bis(*N*2-hexyloxalamide), henceforth abbreviated as **OXA3,6**, was synthesized in a two-step condensation reaction through the dropwise addition of a solution 1,3-diaminopropane (7.4 g, 0.1 mol) in THF (60 mL) to a 10-fold excess of diethyloxalate (146 g, 1 mol). The intermediate product, ethyl 2-[3-[(2-ethoxy-2-oxoacetyl)amino]propylamino]-2-oxoacetate (**OXA3**), was allowed to precipitate during the reaction at room temperature for 24 h, after which it was isolated through filtration. Next, the product was dissolved in chloroform, heated, and hot filtered. White **OXA3** powder was obtained after the evaporation of the chloroform solvent from the filtrate. In the second reaction step, 5 g of **OXA3** was dissolved in 200 mL of chloroform together with 3.7 g of hexylamine, and the mixture was left to stir under refluxing conditions for 48 h. The final product **OXA3,6** was isolated through filtration, followed by washing with chloroform (2×) and diethyl ether (2×) and drying *in vacuo* at 80 °C overnight. The pure **OXA3,6** displayed a melting temperature of 231 °C as observed in DSC analysis performed at a heating rate of 10 °C/min.[10] Similar to the crystallization behavior displayed in Figure 1B, the melting temperature of **OXA3,6** crystallites is suppressed when blended in *i*PP. Melting is observed at a constant heating rate of 10 °C/min in polarization optical microscopy mounted with a Linkam hotstage at 185, 205, and 210 °C for blends having a concentration of 0.25, 0.5, and 1.0 wt % **OXA3,6**, respectively. The polypropylene used in this study was Borealis *i*PP (HD234CF grade). Prior to processing, all materials were dried overnight *in vacuo* at 80 °C. All samples (having various concentrations of **OXA3,6**) were extruded in a twin-screw extruder (DSM Xplore MC 5, 5 mL barrel) at 220 °C for 3 min at 100 rpm. The extrudate was directly injection molded into rheometer plates (2 mm thickness, 25 mm diameter) using a DSM Xplore, IM 5.5 microinjection molder. Furthermore, a second batch of polymer was processed following the same protocol, except that these were compression molded and cut into bars of 1.5 × 6 × 160 mm³ that fit into the slit-flow device.

Characterization Methods. The linear viscoelastic behavior (*G*′ and *G*″) of the samples was determined using a TA Instruments Discovery HR 1 rheometer mounted with a parallel plate geometry (25 mm). Samples were loaded at 180 or 220 °C and cooled to 150 °C at a rate of 5 °C/min using a temperature ramp (1 rad/s, 1% strain). Next, the sample was heated to 250 °C at a rate of 5 °C/min,
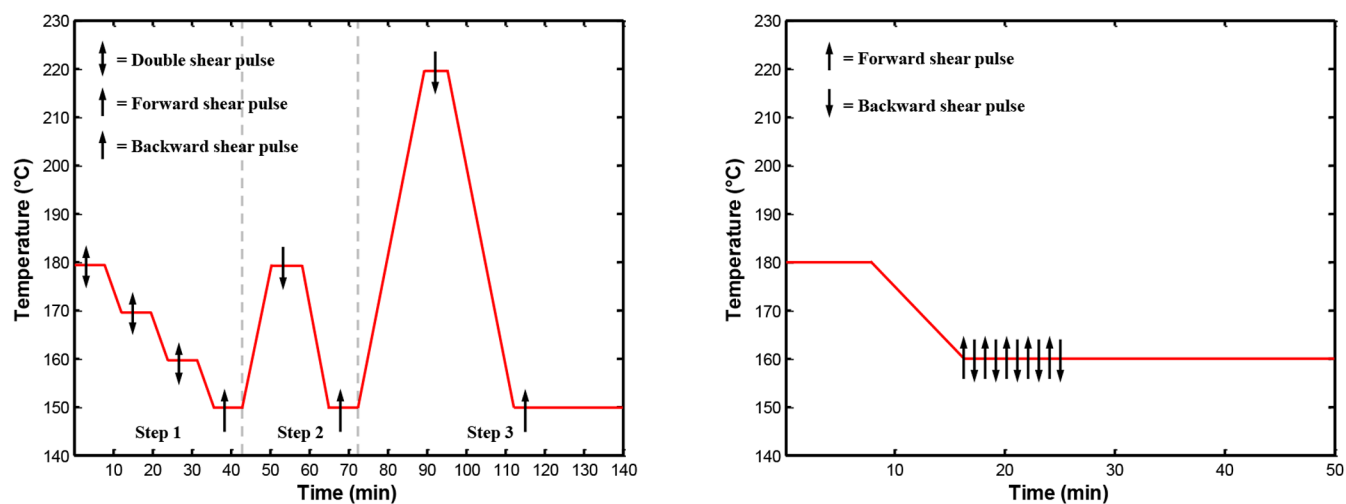
Figure 2. Experimental protocols used in slit-flow experiments.

whereas a frequency sweep was performed every 10 °C (1% strain). Note that frequency sweeps were only taken at 160 °C and higher as slow crystallization proceeded during frequency sweeps performed at 150 °C.

Polarization optical micrographs (between cross-polarizers and using a 530 nm λ-wave plate) were taken on an Olympus BX53 microscope mounted with an Olympus DP26 camera and a Linkam hotstage. The samples were heated to 220 °C at a rate of 30 °C/min and kept for 5 min under this condition. Next, the samples were cooled to 180 °C at a rate of 1, 5, or 30 °C/min to induce the crystallization of **OXA3,6** into rhombic crystallites with various sizes. In some cases, to identify what happens to the **OXA3,6** particles when subjected to shear stress, the sample was subjected to mild shear by hand after reaching 180 °C, and the optical morphology was monitored.

Online 2D small-angle X-ray scattering (SAXS) and wide-angle X-ray diffraction (WAXD) experiments (wavelength = 0.1 nm), following the morphological development during and after the flow, were performed in the European Synchrotron Radiation Facility (ESRF) at the DUBBLE beamline (BM26B, Grenoble, France). This beamline is particularly optimized for polymer science and allows for the installment of the slit-flow device, as is reported by Bras et al.[31] and Portale et al.[32] SAXS images were collected with a 2D Pilatus 1M detector (169 mm × 179 mm active area) placed at 3.50 m distance from the sample, whereas the WAXD images were collected using a Pilatus 300K detector (1472 × 195 pixels of 172 μm × 172 μm) at a distance of 0.21 m from the sample. The detector was triggered by an electric TTL pulse at the start of the displacement of the pistons to synchronize the data acquisition. The data were background corrected and normalized for synchrotron beam fluctuations using an ionization chamber placed before the sample. Furthermore, correction for sample absorption was performed using a photodiode located at the beamstop. Both silver behenate and aluminum were used to calibrate the modulus of the scattering vector q-scale, using the position from diffraction peaks where $q = 4\pi \sin \theta / \lambda$ with θ being half of the scattering angle.

Shear and Crystallization Protocols Using Slit-Flow Experiments. As is highlighted in Figure 1B, the phase behavior of **OXA3,6** in iPP under quiescent conditions has already been reported. However, as mentioned in the Introduction, the nucleation efficiency of iPP in the presence of **OXA3,6** and shear is significantly enhanced, although the exact origin is unknown. To accurately assess the effect of both shear and **OXA3,6** on the viscoelastic response of iPP, slit-flow experiments were performed in the melt using a slit-flow device.[33] In this setup, the polymer is confined between two hydraulically driven pistons. Slit-flow experiments are performed by moving both pistons in the same direction. Similarly, pressurization of the polymers is imposed by moving the pistons toward each other,

whereas the pressure is controlled up to 1000 bar and monitored by two pressure transducers. These pressure transducers are also used to monitor the pressure difference during slit-flow experiments. The structure development of the polymer upon slit-flow experiments is monitored *online* using X-ray diffraction through the two diamond windows having a 60° opening located in middle of the slit.

Through the application of shear pulse at different temperatures we assessed the effect of shear on the rheological behavior (Figure 7) and structure development of iPP when **OXA3,6** resides in the molten or crystalline state. Additionally, through the application of a series of pulses on the iPP melt, we can in turn assess how shear affects both the **OXA3,6** particles and iPP shish formation. To probe these parameters, two slit-flow protocols were performed in this study: In the first slit-flow protocol we probe the effect of different thermal and shear histories on the behavior of the **OXA3,6** crystallites and the resulting shish formation (Figure 2, left). In the second slit-flow protocol we probe the effect of the application of consecutive shear pulses at 160 °C on the shish formation and the development of the resulting shish-kebab morphology (Figure 2, right).

In more detail, slit-flow protocol 1 involves the application of a shear pulse at 150 °C (all pulses were 15 mm at 100 mm/s equaling an apparent wall shear rate $\dot{\gamma}_{wall}$ of 400 s^{-1}) after introducing three different thermal and flow histories: In the first step, the sample is loaded and heated to 180 °C to maintain the thermal history and **OXA3,6** crystallite morphology induced during processing (i.e., **OXA3,6** crystallites in samples having a concentration of 0.5 and 1.0 wt % **OXA3,6** melt well above 180 °C). The sample is pressured to 50 bar, and a backward and forward shear pulse were given after a 3 min isotherm. The structure development was monitored over a period of 5 min. Next, the sample was cooled at a rate of 5 °C/min to 170 and 160 °C, where the same shear protocol was applied after reaching both temperatures. Lastly, in this step the sample was cooled to 150 °C after which a forward pulse was given and the shear morphology was monitored. Note that in this step of the protocol we do not melt the material in between shear pulses, indicating that we do not erase the flow history introduced at higher temperatures. The second step of the protocol involves the melting of the iPP crystallites formed at 150 °C without the melting of the **OXA3,6** particles. This is done through heating to 180 °C, the application of a backward pulse to reset the slit-flow device, leaving the sample again for a 3 min isotherm. Now, the sample is immediately cooled to 150 °C, followed by a 3 min isotherm and a forward pulse. In the third step of this protocol, the sample is heated to 220 °C to erase all shear history *and* to melt the **OXA3,6** particles. Upon reaching 220 °C, again a backward pulse is applied to reset the slit-flow device, followed by a 3 min isotherm. Next, the sample was cooled to 150 °C, a forward shear pulse (15 mm at 100 mm/s) was applied, and the structure development was monitored again for 5 min.

The second slit-flow protocol involves heating the sample to 180 °C to melt the iPP crystallites without melting the NA morphology introduced during processing. Next, the samples were cooled directly to 160 °C, after which a series of 10 shear pulses (5 forward and 5 backward pulses of 15 mm at 100 mm/s) were given with 1 min intervals. After the application of the 10 shear pulses, the sample was kept isothermal in order for iPP crystallization to proceed. Throughout this protocol, the structure development was monitored.

■ RESULTS AND DISCUSSION

Viscosity Suppression of iPP in the Molten State of OXA3,6. The iPP grade used in this study (Borealis HD234CF) has an average molecular weight (M_w) of 310 kg/mol and a dispersity of M_w/M_n = 3.4 and was selected because its viscoelastic and shear responses have been extensively studied in the past.[34−37] To evaluate the effect of **OXA3,6** on the linear viscoelastic response of this iPP grade, samples have been prepared with 0.25, 0.5, and 1.0 wt % **OXA3,6**. The samples were loaded in the rheometer at 220 °C to enforce melting of the **OXA3,6** particles. A frequency sweep was performed after a 3 min isotherm under these conditions. Figures depicting the elastic modulus G', the viscous modulus G'', and the phase angle of the frequency sweeps performed in this study are provided in the Supporting Information. From Figure 3 it is apparent that the plateau in complex viscosity for
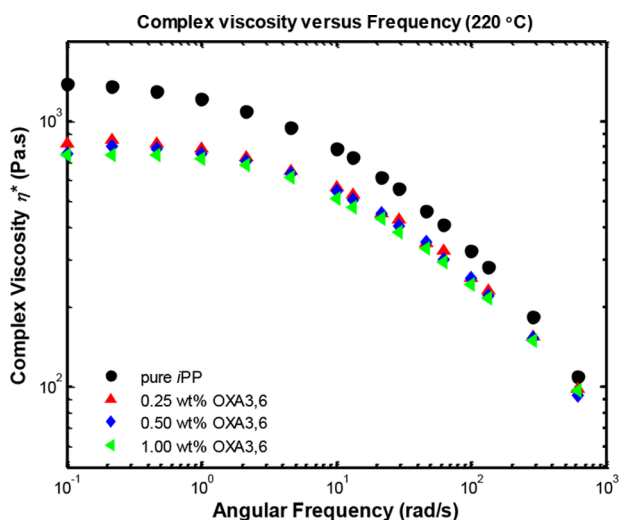
Figure 3. Complex viscosity versus frequency for iPP containing various amounts of **OXA3,6** determined at 220 °C. Note that two frequency sweeps are depicted per sample representing the high and low frequency range.
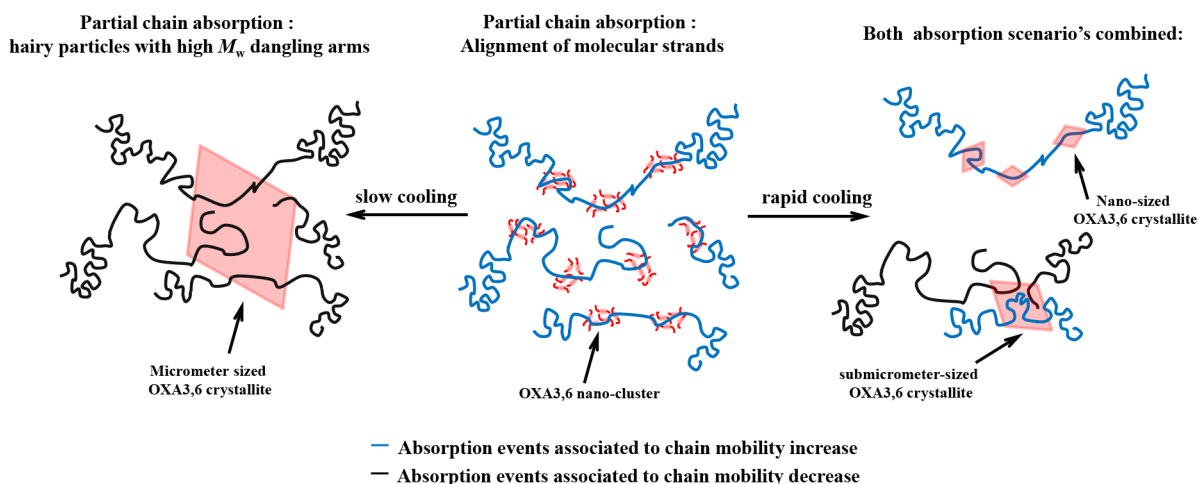
the pure iPP sample is roughly 50% higher at 220 °C compared to the samples having **OXA3,6**. Additionally, it may be concluded that at 220 °C the complex viscosity decreases slightly with increasing **OXA3,6** concentration throughout the evaluated frequency range. In line with previous observations,[23] these findings confirm that **OXA3,6** facilitates a viscosity suppression in iPP.

A comparable viscosity suppressing effect has been reported for polymers in the presence of solid nanofillers.[9] The difference in the viscosity suppression observed in this study is that it is facilitated while **OXA3,6** is present in the molten state. Furthermore, the effect of **OXA3,6** on the viscoelastic response of iPP is distinctly different from those observed in nanoparticle filled systems. As will be supported with slit-flow experiments, plate−plate rheometry, and polarized optical

microscopy, **OXA3,6** can facilitate both a suppression and enhancement of the viscoelastic response of iPP by a variation of the cooling rate while maintaining a constant **OXA3,6** concentration. In contrast, the viscosity suppression in nanoparticle filled systems is only dependent on the concentration at a given particle size. What follows is a step by step explanation of the hypothesis, schematically represented in Figure 4, explaining both the viscosity suppressing and enhancement mechanism of iPP by **OXA3,6**.

With respect to the viscosity suppression, earlier, with the help of molecular modeling, we concluded that the **OXA3,6** concentration is far too low to facilitate the observed enhancement in molecular relaxation, thus excluding the possibility that **OXA3,6** acts as a solvent for iPP.[23] This implies that there should be some sort of interaction between the **OXA3,6** molecules and the iPP chains, where the average effect is the speed-up of the chain dynamics, especially the large scale reorientation of the chains (i.e., in the terminal regime). According to the data provided in Figure 3, this interaction should not cause any significant disruption of the entanglement network. In polymer melts containing solid nanoparticles, the viscosity suppression has been interpreted as full withdrawal (absorption) of polymer chains on the particles.[9] Considering that iPP chains in this study are substantially entangled, full chain absorption would seem improbable in particular for the high molecular weight chains in the upper part of the molecular weight distribution.

Instead, we consider that **OXA3,6** molecules do not fully dissolve in iPP upon melting but instead persist as nanosized clusters held together by weak hydrogen bonding persisting above the **OXA3,6** melting temperature, an hypothesis in accordance with hydrogen bonding in aliphatic polyamides above their melting temperature.[38,39] In other words, following this hypothesis, when dissolved in iPP and above the **OXA3,6** melting temperature, **OXA3,6** persists as nanosized domains having only short-range order, rather than residing in a fully amorphous state. We speculate that the typical size of a nanocluster is somewhat smaller than the size of the entanglement mesh (tube diameter), meaning that it should contain only few (of the order of ten) **OXA3,6** molecules. As a result, a nanocluster can diffuse distances of the order of the size of a typical iPP chain with molecular weight M_w (310 kg/mol) much faster than the iPP chain itself. In this respect, within the experimental time window, it can interact with numerous iPP segments of different chains. We hypothesize that the interaction suppresses the viscosity in the following manner: The affinity between the hexane end-groups of **OXA3,6** and iPP segments as well as the loose arrangement of the clusters facilitates absorption/attachment of iPP segments (or small chain sections of size M_e, the entanglement molecular weight). These absorbed segments temporarily carry some extra friction. Thus, molecular strands between absorbed segments can orient and stretch slightly. The segmental absorption is expected to be weak, meaning that it has a transient nature. Following the detachment of a nanocluster, the oriented strands will tend to rapidly rearrange themselves in a less aligned fashion. It should be noted that not all (partial) absorption events will produce the same degree of alignment. Furthermore, some events might produce alignment in directions other than the tube contour. In this respect, we consider that the observed viscosity suppression reflects the average effect of numerous absorption and detachment events occurring in the melt. Overall, the aforementioned interaction

Partial chain absorption :
hairy particles with high M_w dangling arms

Partial chain absorption :
Alignment of molecular strands

Both absorption scenario's combined:

slow cooling

rapid cooling

Nano-sized
OXA3,6 crystallite

Micrometer sized
OXA3,6 crystallite

OXA3,6 nano-cluster

submicrometer-sized
OXA3,6 crystallite

— Absorption events associated to chain mobility increase
— Absorption events associated to chain mobility decrease

Figure 4. Schematic representation of (left) micrometer sized **OXA3,6** crystallites formed during slow cooling. Partial absorption of *i*PP chains leads to a decrease in chain mobility. Crystallites are localized in space, and the absorbed chains partially reorient via CLF. (middle) Partial absorption events leading to increase of chain mobility through molecular alignment. The **OXA3,6** nanoclusters diffuse length scales of the average radius of gyration much faster than the *i*PP chains themselves do. (right) Formation of **OXA3,6** crystallites of nano- and submicrometer size during rapid cooling. Nanocrystallites can contribute to the increase in chain mobility in a similar manner to nanoclusters. However, the larger crystallites have reduced mobility, effectively resulting in a decrease in the rate of absorption events responsible for the enhanced chain mobility. Furthermore, they might localize *i*PP chains, arresting their large scale reorientation. Note that the *i*PP chains in the bulk are not shown in this image.
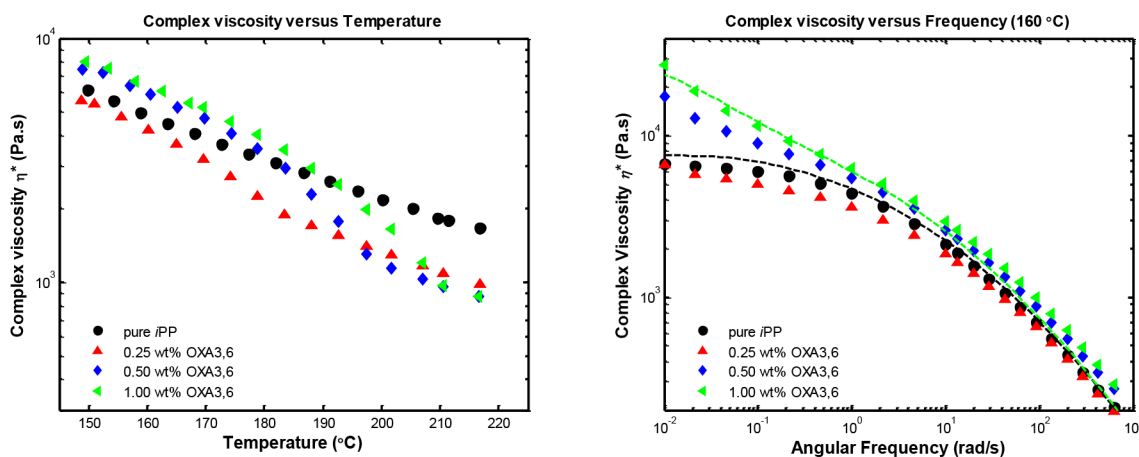
Figure 5. (left) Temperature dependence of the complex viscosity for *i*PP containing various amounts of **OXA3,6** during cooling from 220 to 150 °C at a rate of 5 °C/min, taken at a frequency of 1 rad/s and 1% strain. (right) Complex viscosity versus frequency for *i*PP containing various amounts of **OXA3,6** determined at 160 °C. The black (pure *i*PP) and green (1.0 wt % **OXA3,6**) dotted lines show the predicted values of the complex viscosity obtained from the tube model, according to the scenario visualized in Figure S1A.

between dynamic **OXA3,6** nanoclusters and *i*PP segments induces partial molecular alignment to the chains which, in turn, causes reduction of the chain friction and thus a speed-up of chain dynamics. Molecular alignment is known to reduce the chain friction at fast flows.[40] An alternative way to comprehend the proposed mechanism is to envisage a chain with an effective molecular weight that is slightly lower than the actual molecular weight. Figure 4, middle image, is an illustration of the proposed mechanism.

From the aforementioned theoretical standpoint, the fact that the viscosity suppression increases with decreasing frequency (as can be observed from Figure 3) reflects the cumulative effect that the faster relaxation of shorter chains has on the relaxation of longer chains. That is, the **OXA3,6** clusters speed up the relaxation of a chain of given M_w with respect to its relaxation in the pure *i*PP melt. In turn, this speed-up mediates a faster relaxation of chains of higher molecular

weight through ordinary constraint release. The interaction of **OXA3,6** nanoclusters with molecular segments of the latter chains enhances the chain's dynamics over and above the former speed-up. Furthermore, with increasing dilution of the entanglement network, aligned strands of one chain might induce alignment on strands of neighboring chains.

Another possibility for the observed suppression in viscosity involves migration of **OXA3,6** nanoclusters to the sample surface, facilitating slip with the rheometer plates during the experiments. However, the slit-flow experiments explained later in this work do not support this scenario.

Contribution of OXA3,6 Crystallites to the Viscoelastic Response of *i*PP. The observation of a viscosity enhancement of *i*PP by **OXA3,6** requires the **OXA3,6** to crystallize during cooling. Therefore, to investigate the influence of the crystallization of the **OXA3,6** nanoclusters on the viscoelastic response, **OXA3,6** nuclei were seeded by

cooling the samples from 220 to 150 °C (Figure 5, left). Subsequently, the samples were heated to 160 °C and were subjected to a frequency sweep (Figure 5, right) under isothermal condition. As anticipated, a stepwise increase in the complex viscosity is observed on cooling the sample from 220 to 160 °C. The viscosity increase upon cooling of pure iPP solely reflects the temperature dependence of unperturbed reptation dynamics. However, in the presence of OXA3,6 the viscosity of the polymer melt exhibits a more abrupt upturn, which is related to the formation of OXA3,6 crystallites. From Figure 5 (left) it is evident that the effective increase in complex viscosity upon crystallization of OXA3,6 is dependent on the OXA3,6 concentration; the higher the OXA3,6 concentration, the larger is the stepwise increase in complex viscosity. In addition, in accordance with Figure 1B, with increasing OXA3,6 concentration, the onset of crystallization of OXA3,6 particles proceeds at higher temperatures. For example, the OXA3,6 crystallizes at 180, 195, and 210 °C for iPP samples containing 0.25, 0.5, and 1.0 wt % OXA3,6, respectively.

From the viewpoint of the partial absorption scenario presented above, the findings of Figure 5 can be qualitatively explained as follows. For a given concentration, the OXA3,6 supersaturation, and thus the tendency to nucleate and crystallize, becomes larger with decreasing temperature. In other words, the ability of different nanoclusters to nucleate or aggregate into larger nanoclusters or crystallites increases. Thus, starting from the melting temperature, there is a temperature window where the average size of the formed OXA3,6 crystallites is still comparable to the size of the entanglement network; such nanoparticles can still contribute to the viscosity suppression through alignment of molecular strands. However, as crystal growth proceeds with decreasing temperature, their mobility drops as entanglements are influencing their diffusion. As a result, the overall frequency of partial absorption events decreases; such events begin to attain a local character, thereby influencing the configurations of fewer chains. Thus, compared to the pure melt, the overall effect might be a viscosity decrease or increase, depending on the average OXA3,6 crystal size (Figure 4, right). Upon further cooling, more and more nanoclusters will be taken up in the growing crystallites, which can reach micrometer dimensions if enough time is given. In this regime, the overall effect is a viscosity increase (relatively to the pure iPP melt) since a fraction of iPP melt chains has molecular segments absorbed on crystals that have dimensions much larger than the size of the chain (Figure 4, left). Moreover, the crystals are localized in space. Recall, however, that the weight fraction of OXA3.6 is very low; hence, we consider it unlikely that the viscosity increase, relative to the melt without OXA3.6, does originate from the crystals themselves. Instead, it arises from the slowdown of the molecular motions of the iPP chains that are partially absorbed on the crystals' surface. With increasing concentration, the crossover to the regime of higher viscosity occurs at higher temperatures because crystals with dimensions beyond the nanoscale are formed already at higher temperatures.

Interestingly, for the sample having 0.25 wt % OXA3,6 the complex viscosity after OXA3,6 crystallization is still lower than that of the pure iPP. In contrast, the complex viscosity for samples having 0.5 and 1.0 wt % OXA3,6 surpasses the complex viscosity of the pure iPP throughout the evaluated frequency range (Figure 5, right). Moreover, at low frequencies

a further increase in complex viscosity is observed, originating from the onset of a plateau in the elastic modulus (Figure S4). The origin of the plateau in elastic modulus can originate from (1) a bridging effect of iPP chains absorbed on the different OXA3,6 particles,[29] (2) the presence of long dangling iPP arms resulting from the physical absorption of iPP molecular segments on the OXA3,6 crystallites, or (3) a percolated network of OXA3,6 particles.[41]

The OXA3,6 rhombic crystallites grown under the conditions applied in the rheometer experiments are found to have a diagonal length of 10 μm (according to optical observations in between cross-polars presented in Figure S5). For comparison, the average radius of gyration of the polypropylene used in this study is 21.7 nm (estimated using $R_g/M_w^{(1/2)} = 0.039$ nm).[42] Given this mismatch in length scales of the OXA3,6 crystallites and iPP coil sizes, we rule out the possibility of the iPP chains bridging the OXA3,6 crystallites.

The second possibility is in accordance with the partial absorption picture introduced above and schematically represented in Figure 4, left. When large rhombic crystallites are formed, the absorption of iPP molecular segments arrests reptative reorientation modes: Large-scale reorientation of the chains is frozen. Hence, the resulting OXA3,6 crystallites are expected to behave as starlike polymer chains or hairy particles in terms of their rheological response.[43−45]

In this scenario, the absorbed chains will contain long dangling arms. Such long dangling arms renew their orientation via contour length fluctuations (CLF) rather than reptation. For highly entangled chains, it is well established that the CLF relaxation mechanism is dramatically slower than reptation since the relaxation (reorientation) time of a chain segment along an arm has an exponential dependence on the arm molecular weight.[46,47] Such slowdown of the chain dynamics can give rise to the appearance of a broad shoulder or even a second plateau in the terminal regime.[48,49] Therefore, considering that chains in our systems have high molecular weights (recall $M_w = 310$ kg/mol, corresponding to 60−70 entanglements per chain), we anticipate a strong retardation in the terminal relaxation of the systems containing large, micrometer-sized NA crystallites. To support this hypothesis further, we used molecular modeling[46] to examine how the viscoelastic response changes in the presence of long dangling arms for the melt having 1.0 wt % OXA3,6. The system having 1.0 wt % OXA3,6 was chosen due to its larger NA concentration and should thus lead to a higher degree of absorption of chains having long dangling arms. As readily seen in Figure 5, right (green dashed line), the presence of a low volume fraction (i.e., 10%) of long dangling arms indeed changes the linear viscoelastic response significantly. At low frequencies, an upturn in the complex viscosity is predicted in agreement with the experimental data (green symbols). The agreement is not quantitative because the exact volume fractions and molecular weight distribution of the (bulk) linear chains and the dangling ends of the absorbed chains are unknown: The value of 10% was used as an estimate since the exact volume fraction of dangling arms is unknown. The same applies to the molecular weight distribution of the arms; thus, the latter was constructed from the high molecular weight tail of the pure iPP melt (see the Supporting Information for more details). Concerning the pure iPP melt, the tube model matches the experimental data (black solid line, Figure 5, right) by considering reptative dynamics. Note that the
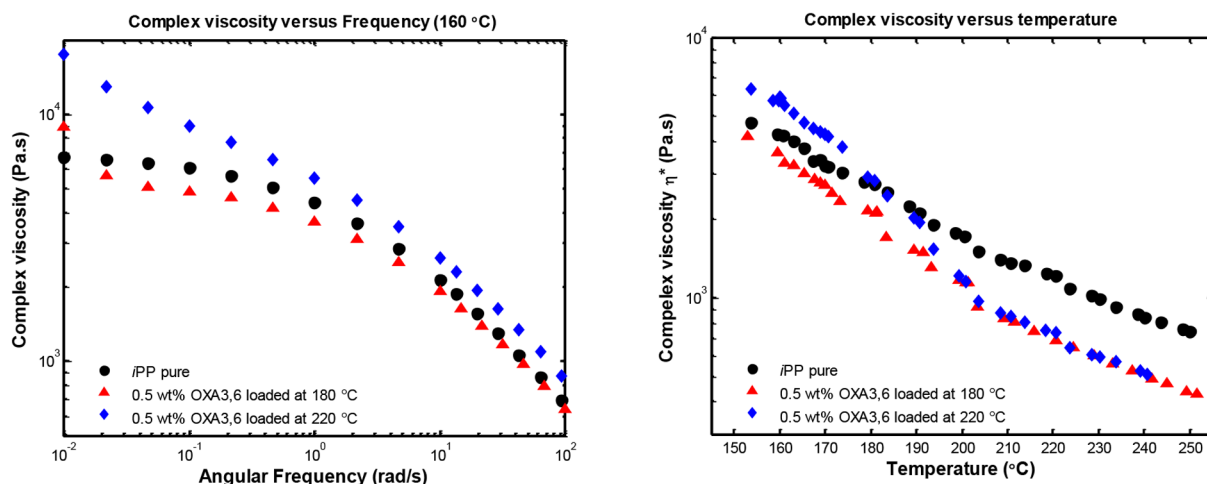
Figure 6. Effect of thermal history on the viscoelastic behavior for *i*PP containing 0.5 wt % **OXA3,6** (left) and the temperature dependency of the complex viscosity as a function of thermal history, taken at a frequency of 1 rad/s and 1% strain (right). Note that the samples with **OXA3,6** were loaded at 180 and 220 °C, whereas the iPP sample was loaded at 220 °C. All samples were cooled to 150 °C at a rate of 5 °C/min, followed by heating to 160 °C and a frequency sweep.

parametrization used to obtain the theoretical predictions in Figure 5 is consistent with the one used in our earlier work.[23] Overall, the predictions of the tube model support the possibility that long dangling *i*PP arms on **OXA3,6** crystallites are responsible for the rise in the low-frequency plateau in elastic modulus in the presence of **OXA3,6** crystallites.

When the origin of the elastic plateau in the terminal regime is the result of such long *i*PP arms absorbed on **OXA3,6** particles, we can expect that this behavior is triggered at a critical **OXA3,6** particle size. As explained earlier, this critical particle size appears to be of order of the radius of gyration of the high molecular weight *i*PP chains. Apart from the **OXA3,6** concentration, the net contribution of the **OXA3,6** crystallites will also be dependent on the thermal history. These two factors together govern the crystallite nucleation and growth process. With respect to the thermal history, on slow cooling, the initial nucleation rate of **OXA3,6** crystallites will be low due to the low undercooling. As is visible from Figure 1C, such low nucleation density results in the growth of large **OXA3,6** crystallites. The number of nuclei will increase during further cooling, eventually resulting in a distribution of **OXA3,6** crystallites with varying but large size. Indeed, as observed from Figure 5, right, and Figure S5, systems with large **OXA3,6** crystallite size facilitate a strong increase in viscosity compared to pure *i*PP. Similarly, subjecting the sample to high cooling rates increases the nucleation density of **OXA3,6** due to the rapid achievement of high undercooling, yielding a large number of small **OXA3,6** crystallites (Figure 1C) with a net viscosity decrease compared to the *i*PP, as reported in earlier work.[23]

With respect to the used **OXA3,6** concentration, as is visible from Figure 1B, increasing the **OXA3,6** concentration increases the temperature where crystallization proceeds, thereby decreasing the nucleation density (lower supersaturation) and thus favoring the growth of large **OXA3,6** crystallites.[10] Indeed, this feature is detected in our samples: The usage of 0.25 wt % **OXA3,6** apparently yields sufficiently small crystallites to facilitate a net viscosity suppression compared to the pure *i*PP (Figure 5, right). In contrast, increasing the **OXA3,6** concentration to 0.5 or 1.0 wt %

increases the crystallite size such that it favors the generation of dangling *i*PP arms and the concomitant viscosity enhancement.

To assess the third possibility for the elastic network in the terminal regime (i.e., the presence of a percolated network of **OXA3,6** crystallites), we examine whether a reduction of particle size leads to an increase in elasticity. As has been reported by Hao and co-workers,[50] the critical concentration for the generation of a particle network is achieved at lower concentrations when using particles with smaller size. Consequently, decreasing the particle size in an already percolated network should increase the elastic modulus of the particle network. To relate this finding to the current scope, recall that the samples were prepared in an extruder at 220 °C, after which they were injection molded into rheo-discs. The high shear and cooling rates applied during injection molding result in **OXA3,6** particles with submicrometer dimensions as they are barely detectable in polarization optical microscopy (Figure S5). In practice, the samples having 0.5 and 1.0 wt % **OXA3,6** could be loaded in the rheometer at 180 °C without melting the **OXA3,6** particle morphology generated during processing. Therefore, loading the samples at 180° allows us to probe the effect of **OXA3,6** crystallites with a significantly decreased size compared to when they are crystallized during cooling after loading at 220 °C. Once loaded in the rheometer, the materials were cooled to 150 °C, after which they were subjected to the same protocol as the samples loaded at 220 °C (i.e., heated to 160 °C, followed by a frequency sweep).

As is shown in Figure 6 left, loading the sample having 0.5 wt % **OXA3,6** at 180 °C, i.e., maintaining the fine **OXA3,6** particle morphology generated during processing, yields in fact a lowered viscoelastic response compared to the pure *i*PP. The fact that a decrease in particle size results in a significant suppression in viscoelastic response excludes the possibility for the presence of an **OXA3,6** particle network under the evaluated conditions. Instead, these findings favor the hypothesis that physical absorption of *i*PP segments on the **OXA3,6** crystallite surface determines the viscoelastic response of the melt for two reasons: (1) the viscosity of the sample is lower than the pure *i*PP, suggesting that the **OXA3,6** crystallites are sufficiently small to produce an overall
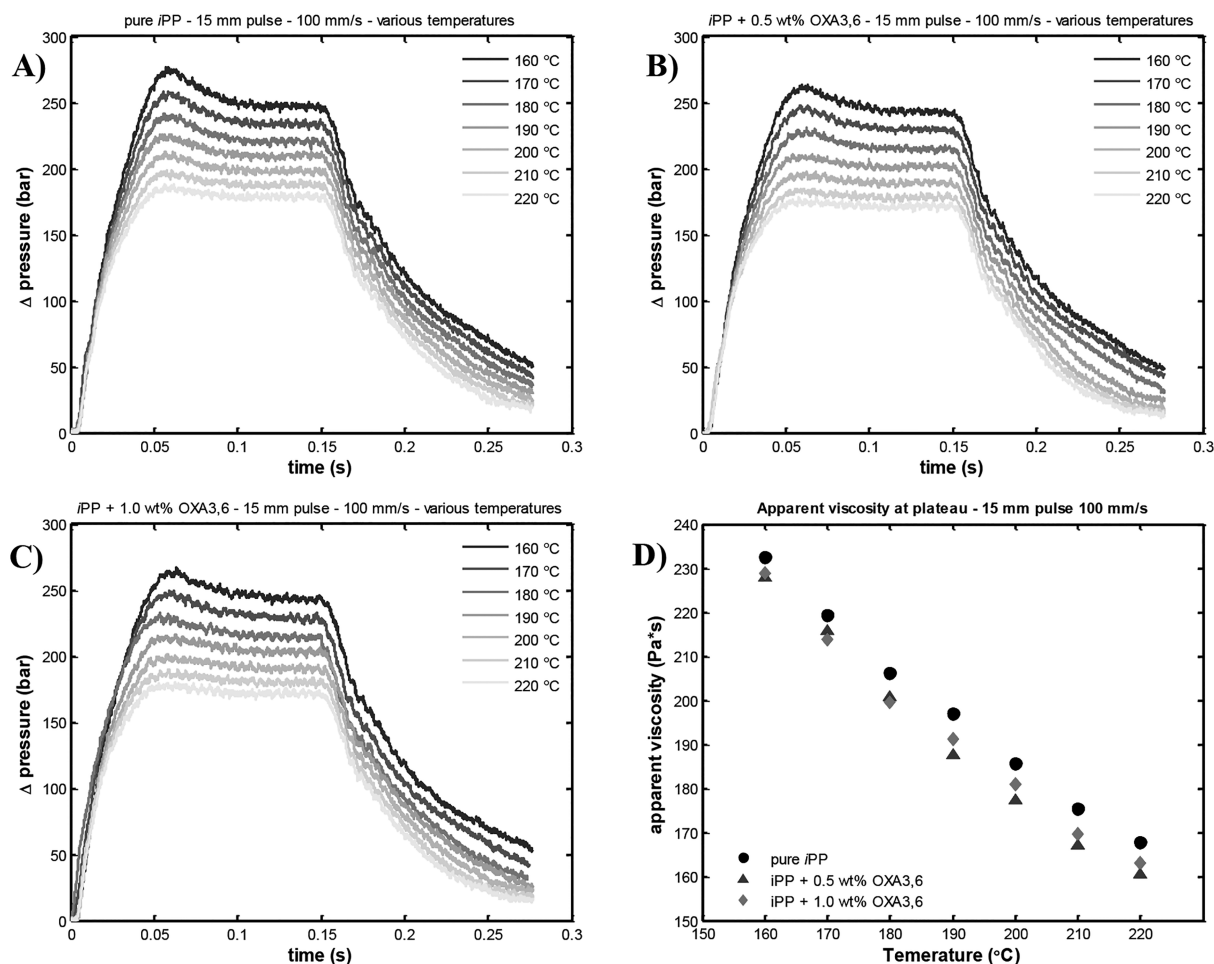
Figure 7. Pressure difference (ΔP) observed during the application of shear pulses at various temperatures for pure iPP (A), iPP + 0.5 wt % **OXA3,6** (B), and 1.0 wt % **OXA3,6** (C). Image (D) depicts an overview of the apparent viscosity during steady shear extracted from the data in images (A)−(C) using eqs 1−3.

reduction of chain friction via the partial absorption mechanism explained above, and (2) the presence of the onset of a plateau in the elastic modulus at low frequencies (Figure S6) suggests that these **OXA3,6** crystallites also contain dangling iPP arms (hence, this example follows the absorption scenario depicted in Figure 4, right). Similar results are obtained for the sample having 1.0 wt % **OXA3,6**, for which the data are provided in Figure S7.

Although loading the sample at 180 °C results in a lowered complex viscosity compared to the pure iPP at 160 °C, the complex viscosity drops further upon melting of the **OXA3,6** particles. As is shown in Figure 6, right, the complex viscosity of samples loaded at the different temperatures, i.e., samples having a different **OXA3,6** particle size, coincides upon melting of the **OXA3,6** particles and upon further heating. These findings indicate that the viscosity enhancing effect of the dangling iPP arms is lost upon melting of the **OXA3,6** crystallites, irrespective of the thermal history of the sample. Again, similar behavior was observed for the sample containing 1.0 wt % **OXA3,6**, as is shown in Figure S8.

Confirming the Viscosity Suppression in iPP with OXA3,6 Using Slit-Flow Experiments. Slit-flow experiments were performed to identify whether the viscosity suppression in iPP with **OXA3,6** persists during shear experiments. Therefore, samples having 0.5 and 1.0 wt %

OXA3,6 were heated to the desired temperature, and a shear pulse of 15 mm was given at a rate of 100 mm/s to the samples. During the pulse, the pressure difference (ΔP in bar) was monitored, as can be seen from Figures 7A−C. Generally, an initial pressure buildup is observed at the start of the shear pulse until a steady shear plateau is achieved. The pressure difference during the pulse was converted to the apparent viscosity (η) using eqs 1−3:

$$\dot{\gamma} = \frac{6Q}{WH^2} \tag{1}$$

$$\sigma = \frac{H\Delta P}{2\left(1 + \frac{H}{W}\right)L} \tag{2}$$

$$\eta = \frac{\sigma}{\dot{\gamma}} = \frac{H^2}{12\left(1 + \frac{H}{W}\right)L}\frac{\Delta P}{V_{\text{piston}}} \tag{3}$$

where W and H are the slit width and thickness of 6 and 1.5 mm, respectively, Q is the volumetric flow rate being $H \times W \times V_{\text{piston}}$, and L is the distance between the pressure transducers (120 mm).[51] The piston speed (V_{piston}) for shear pulses in this study was fixed to 100 mm/s, corresponding to an apparent shear rate ($\dot{\gamma}$) of 400 s^{-1} (see eq 1). The plateau viscosity during steady shear was plotted as a function of shear

temperature and is shown in Figure 7D. Indeed, in line with previous observations, the **OXA3,6** facilitates a viscosity suppression when it resides in the molten state. Furthermore, at temperatures below 180 °C, the steady shear viscosity of both samples having 0.5 and 1.0 wt % **OXA3,6** start to increase and approach the viscosity of the pure *i*PP sample, which is attributed to crystallization of the **OXA3,6** particles.

Effect of Shear on the OXA3,6 Morphology and Viscoelastic Behavior of *i*PP. Although the viscosity suppression in *i*PP with **OXA3,6** is evident from shear experiments, we have observed that the **OXA3,6** particles are brittle and highly sensitive to folding and breakup during shear (Figure 8). Therefore, to establish a relation between shear, the
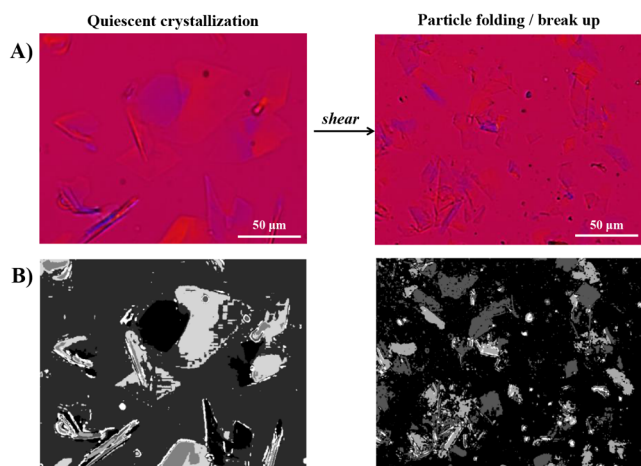
Figure 8. (A) The image on the left depicts the **OXA3,6** particle distribution as observed in polarization optical microscopy after cooling *i*PP containing 1.0 wt % **OXA3,6** from 220 to 180 °C at a rate of 1 °C/min, whereas the image on the right depicts the folding and breakup of the **OXA3,6** particles after drag of the top glass plate at 180 °C. To ease the detection of the characteristic **OXA3,6** particle morphology before and after shear, color-based segmentation has been performed on images (A), whereas the results are depicted in (B).

viscosity suppressing effect, and **OXA3,6** particle breakup, we have subjected the samples to slit-flow protocol 1 described in the Experimental Section. To recall, here we evaluate the effect of shear and thermal history using three different steps: In the first step we load the material at 180 °C and introduce thermal history to the sample through the application of consecutive shear pulses during cooling (i.e., pulses are given at 180, 170, 160, and 150 °C). In the second step, the sample is heated to 180 °C to erase the previously introduced thermal history while preventing the melting of the generated **OXA3,6** particle morphology. After a 3 min isotherm, the sample is cooled to 150 °C, after which another shear pulse is given. The third and last steps of this protocol involve the removal of the thermal history of the sample *and* melting of the **OXA3,6** crystallites through heating to 220 °C. Again, the samples are cooled to 150 °C, after which the last shear pulse is given.

Figure 9 shows the 2D-SAXS signals depicting the equatorial scattering region obtained directly after the consecutive shearing steps performed in the first step of slit-flow protocol 1. In general, the application of these shear pulses does not result in the generation of any notable SAXS signal for the pure *i*PP. In contrast, for both the samples containing 0.5 and 1.0 wt % **OXA3,6**, a streak in the equatorial scattering intensity

appears after applying a shear pulse at 170 °C and develops further upon application of the following shear pulses. Such a streak in equatorial scattering intensity suggests the presence of nanosized entities aligned along the shear direction, possibility originating from shear-induced *i*PP shishes or from the **OXA3,6** particles themselves. Further cooling to 150 °C and the application of shear yields the characteristic shish-kebab morphology for all three samples, where the presence of kebabs is deduced from the lobes in vertical scattering intensity. Interestingly, both signals corresponding to the shishes and kebabs are significantly weaker in the pure *i*PP sample than for the samples containing **OXA3,6**. These findings indicate that despite the lowered apparent viscosity, *i*PP in the presence of **OXA3,6** is more sensitive to undergo shear-induced crystallization.[52]

More information about this shear behavior is obtained from the remainder of the slit-flow protocol: No kebabs are formed during the shear pulse at 150 °C in step 2 of slit-flow protocol 1. This is likely the result from the decreased number of shear pulses applied during cooling in step 2 of in this protocol. More importantly, in contrast to the pure *i*PP sample, heating to 180 °C does not remove the scattering in the equatorial region for the samples containing **OXA3,6**, which explains why it persists after cooling back to 150 °C. Only upon heating beyond 180 °C, a gradual decrease in the equatorial scattering signal is observed in the samples containing **OXA3,6**, until the signal fully disappears above 210 °C, as shown in Figure S9. Although it is reported in the literature that a small fraction of crystallites in shishes can persist above the polymers' nominal melting temperature,[53,54] the equatorial scattering signal from the shear-induced shishes in the pure *i*PP is readily lost when reaching 180 °C. Accordingly, it is not likely that the streak in equatorial scattering intensity in samples containing **OXA3,6** originates from regular shear-induced shishes. Given that melting of **OXA3,6** crystallites also proceeds between 180 and 210 °C as shown in Figure 6 and Figure S8, we consider it more likely that the equatorial scattering signal is related to the **OXA3,6** particles themselves. Furthermore, after cooling from 220 °C and performing the shear pulse in step 3 of slit-flow protocol 1, we only observe a small equatorial streak in the samples containing **OXA3,6**, comparable to that of the shear-induced shishes formed in the pure *i*PP. This indicates that formation of the intense streak in equatorial scattering intensity in the presence of **OXA3,6** requires multiple shear pulses.

A possible explanation for the observed shear behavior can be found in the combined shear alignment and particle breakup of the **OXA3,6** crystallites during shear. As discussed in the previous section, **OXA3,6** is expected to physically absorb *i*PP segments on its surface. **OXA3,6** particles decorated with *i*PP chains are likely to cause a disturbance in the flow field and thereby stimulate shear-enhanced shish formation. In particular, when the **OXA3,6** crystallites break up during shear, it is possible that the absorbed *i*PP chains remain anchored on different **OXA3,6** fragments. Given that the **OXA3,6** fragments for during shear, it is likely that the *i*PP chains anchored on different **OXA3,6** fragments are stretched in the process, effectively facilitating a local bridging effect. Such bridging chains would be excellent precursors for shish growth; hence, **OXA3,6** particle breakup is suggested to facilitate shear-enhanced shish formation. Furthermore, as the bridging chains are anchored to the **OXA3,6** particles, bundles of bridging chains will persist well above the nominal melting temperature of *i*PP and give rise to the previously observed
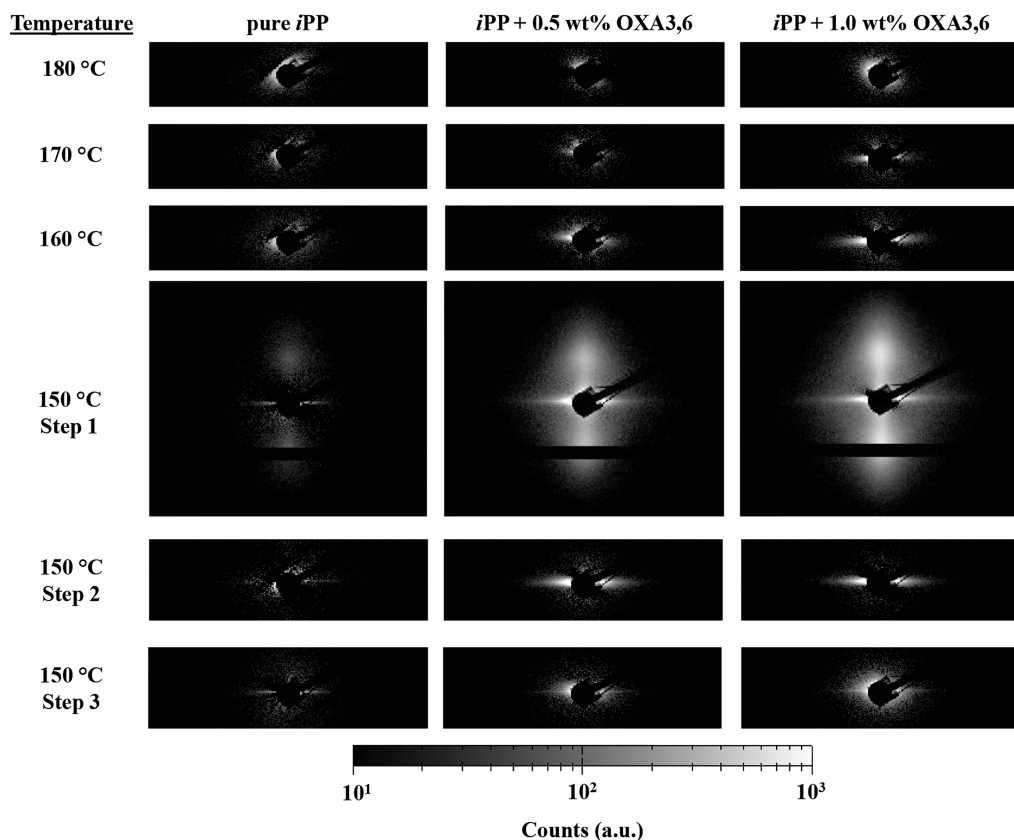
Figure 9. SAXS patterns depicting the equatorial region obtained during the shear pulses at 180, 170, and 160 °C applied in slit-flow protocol 1. Similarly, the SAXS patterns obtained after shearing at 150 °C during the various steps in slit-flow protocol 1 are provided. Note that the images taken directly after the shear pulse applied at 150 °C in step 1 display the full 2D SAXS patterns to visualize the vertical lobes in scattering intensity resulting from the presence of crystal kebabs.
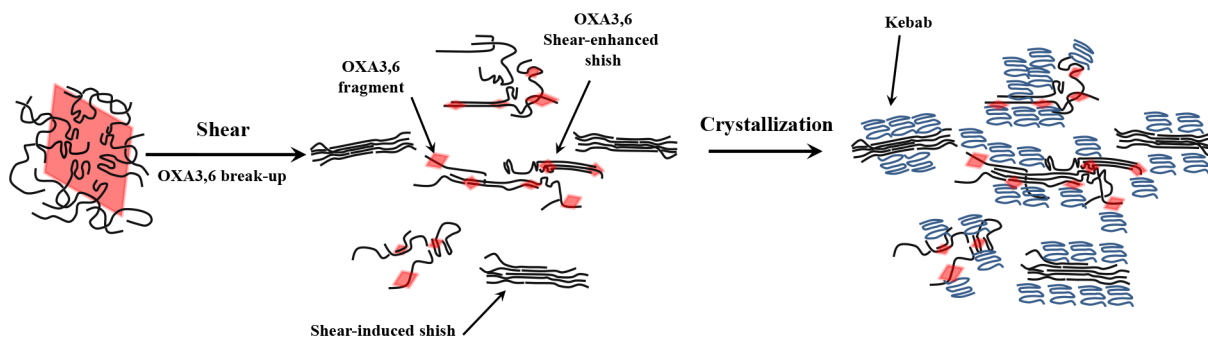

Figure 10. Schematic representation of the shear-induced **OXA3,6** (red rhombic crystallites) fragmentation, resulting in shear-enhanced shish (black bundles) formation through stretching of anchored chains in addition to regular shear-induced shish formation. Additionally, given the nucleating ability of **OXA3,6** particles, they facilitate kebab growth (blue lines) even further.[10]

equatorial scattering signal in SAXS. This signal would only disappear when these stretched chains can relax, i.e., upon the melting of the **OXA3,6** particles, as is in line with our SAXS observations. An example of the proposed mechanism is shown in Figure 10.

To verify this hypothesis, a second slit-flow protocol was performed to obtain more information about how **OXA3,6** affects the *i*PP behavior when subjected to multiple shear pulses. As explained in the Experimental Section (slit-flow protocol 2), samples were loaded at 180 °C, cooled, to 160 °C and subjected to 10 shear pulses with a 1 min interval (5 forward pulses, 5 backward pulses). Figure 11 left shows the

ΔP evolution during the shear pulses performed for the sample containing 1.0 wt % **OXA3,6**. The pulses for the pure *i*PP and the sample containing 0.5 wt % **OXA3,6** are provided in Figure S10. Next, the ΔP during steady shear was converted to the apparent viscosity using eq 3. To highlight the difference in shear behavior, the apparent viscosity of the first *i*PP pulses were subtracted as normalization procedure: The apparent viscosity of the first *i*PP forward pulse was subtracted from the apparent viscosity of all forward pulses, whereas the apparent viscosity of the first *i*PP backward pulse was subtracted from the apparent viscosity of all backward pulses. Figure 11 (right) shows the resulting overview.
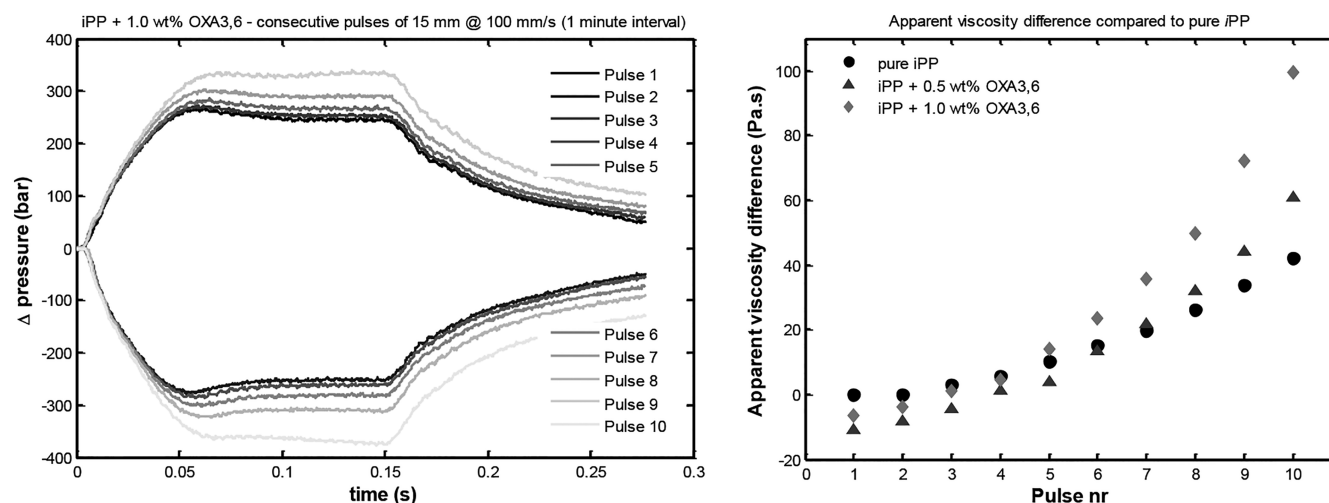
Figure 11. Left: pressure difference (ΔP) observed during the application of the 10 consecutive shear pusles in slit-flow protocol 2, for the sample having 1.0 wt % **OXA3,6**. Right: the apparent viscosity difference calculated from the plateau in ΔP during steady shear using eq 3. Note that only the differences in the presented apparent viscosity values are presented as they are normalized through subtraction of the apparent viscosity of the first forward or backward pulses from the pure *i*PP sample.
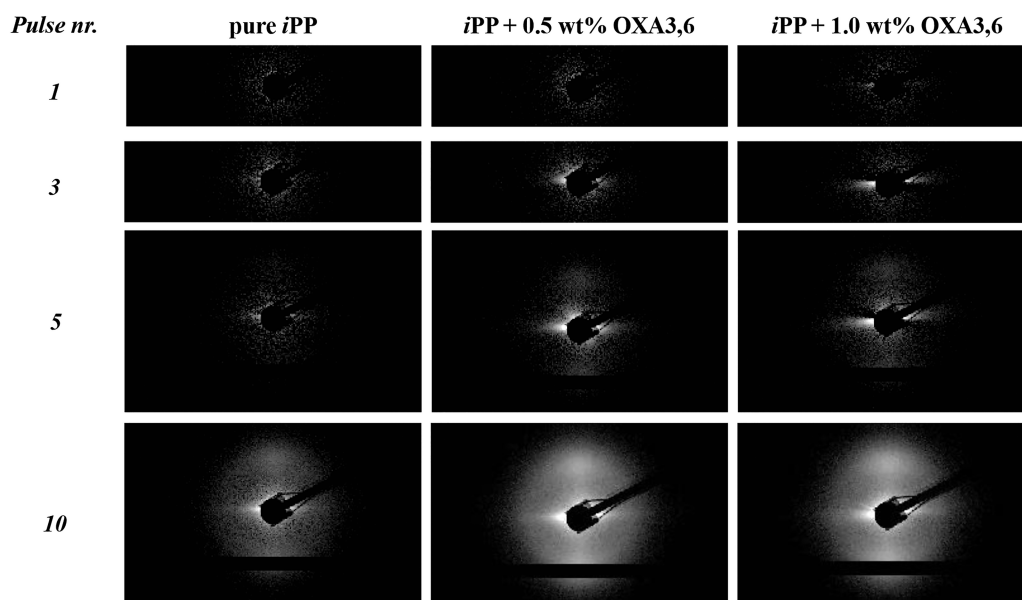
Figure 12. 2D-SAXS patterns obtained directly after the application of shear pulses 1, 3, 5, and 10 applied in slit-flow protocol 2. Note that the scaling of the scattering intensity is the same as used for Figure 9.

For the pure *i*PP sample it can be observed that the steady shear viscosity slowly increases upon the application of the consecutive shear pulses. As is reported in the literature, shear can result in the generation of pointlike nuclei that together with stretched chain segments assemble and grow into a shish when sufficient shear is applied.[3,4] During the application of a shear pulse in the slit flow, the polymer at the wall will be subjected to the highest shear rate and will therefore generate shishes the fastest. As is suggested by Peters and co-workers, these shishes contain polymer chains that are partially embedded in the shish and partially located in the melt; i.e., the shishes are covered in "hairs" that interact with the surrounding melt.[49] During the application of a shear pulse, shishes are generated in sufficient concentration and with sufficient length to macroscopically decrease the fluidity of the sheared layer, thereby decreasing its deformation rate. As a

result, every time a pulse is given in this slit-flow protocol, a small shear layer is deposited at the wall of the sample, effectively decreasing the remaining area for volumetric flow, thus increasing the pressure drop and the viscosity calculated therefrom. Such layer deposition at the wall with application of consecutive shear pulses explains the rather exponential increase in steady shear viscosity observed in the slit-flow protocol 2.

In line with previous observations, we observe that the samples containing **OXA3,6** start with decreased viscosity compared to the pure *i*PP (Figure 11, right). However, upon the application of consecutive shear pulses the ΔP, and thus the viscosity, increases rapidly and surpasses that of the pure *i*PP. The sample containing 0.5 wt % **OXA3,6** exhibits the same steady shear viscosity as the pure *i*PP after six shear pulses. Similarly, the sample containing 1.0 wt % **OXA3,6**

exhibits the same steady shear viscosity as the pure *i*PP already after four shear pulses. This indicates that application of shear in the presence of **OXA3,6** generates thicker shear layers for each applied shear pulse. Indeed, when looking at the 2D-SAXS patterns provided in Figure 12, we can observe similar features as reported in Figure 9 for samples containing **OXA3,6**; the consecutive application of shear pulses results in a rapid development in the streak in equatorial scattering intensity. Furthermore, in line with higher steady shear viscosity and thus the presence of the thicker shear layers, the samples containing **OXA3,6** facilitate a more dominant kebab growth, as is also evident from the 2D-WAXD patterns provided in Figure S11. Additionally, these findings suggest that the suppression in *i*PP viscosity in the presence of **OXA3,6** is facilitated throughout the whole sample: Recall, earlier we mentioned the possibility that the observed viscosity suppression is a result from sample slip originating from **OXA3,6** migrated to the sample surface. Following this scenario, the deposition and immobilization of the first shear-layer in slit-flow experiments should negate this effect as the shear layer is considered immobilized during the following shear pulses. However, this is not the case in our samples; the viscosity suppression in the presence of **OXA3,6** persists during the first 3−5 pulses, indicating that the remaining melt exhibits a decreased viscosity, in particular since the presence of **OXA3,6** results in the generation of thicker shear layers than the pure *i*PP.

Overall, these results are in line with our previous hypothesis: Application of shear in the presence of **OXA3,6** results in significant enhancement in shish formation, followed by the enhanced development of the shish-kebab morphology. Given that the **OXA3,6** particles break up during shear and are presumed to be capable of withdrawing *i*PP segments from the melt through physical absorption, the generation of stretched *i*PP chains between the fragmented **OXA3,6** particles is a plausible origin for this shear-enhanced shish formation. This hypothesis is further supported by the fact that the signal in equatorial scattering intensity, originating from these *i*PP bridges, persists up to the melting temperature of the **OXA3,6** crystallites. It is noteworthy that the shear-enhanced shish formation and the viscosity suppression in the presence of **OXA3,6** have the same origin: They both originate from physical absorption of *i*PP segments on the **OXA3,6** particles.

CONCLUSIONS

In this work we evaluated the influence of thermal history and shear on the melt behavior of *i*PP in the presence of the organic compound **OXA3,6**. We demonstrate that a viscosity suppression is observed in *i*PP when **OXA3,6** resides in the molten state, which we attribute to an effective reduction of chain friction resulting from molecular alignment of *i*PP segments. We argued that the alignment is induced by partial absorption of *i*PP molecular segments on **OXA3,6** nanoclusters present in the melt. However, upon cooling, the **OXA3,6** nanoclusters develop into crystallites having dimensions beyond the radius of gyration of the *i*PP chains and limiting their ability to cause significant reduction of chain friction. Instead, the physical absorption of *i*PP segments on **OXA3,6** crystallites favors the formation of dangling arms, effectively resulting in a viscosity enhancement compared to pure *i*PP and the generation of a plateau in elastic modulus. This effect is amplified when using increasing **OXA3,6** concentrations or slow cooling rates as this increases the

chance for the **OXA3,6** nanoclusters to be taken up in the crystallites. In addition, the application of shear in the presence of **OXA3,6** (1) enhances the shear layer formation, (2) fragments **OXA3,6** crystallites, and (3) gives rise to an equatorial streak in scattering intensity that persists up to the melting of the **OXA3,6** crystallites. This scattering signal is thought to result from a local bridging effect of physically absorbed *i*PP chains that are stretched between the fragmented **OXA3,6** crystallites, resulting in shear-enhanced shish formation and explaining the enhanced shear response.

ASSOCIATED CONTENT

ⓈSupporting Information

The Supporting Information is available free of charge on the ACS Publications website at DOI: 10.1021/acs.macromol.8b02612.

> Additional information about molecular modeling and findings (Figures S1 and S2), rheological behavior of the samples having various thermal history and thus **OXA3,6** sample size (Figures S3−S8), 2D-SAXS images depicting the equatorial scattering intensity of samples containing **OXA3,6** upon heating to 220 °C (Figure S9), development of ΔP during for pure *i*PP and *i*PP containing 0.5 wt % **OXA3,6** during pulses given in slit-flow protocol 2 (Figure S10), WAXD diffractograms in slit-flow protocol 2 (Figure S11) (PDF)

AUTHOR INFORMATION

Corresponding Authors
*E-mail karel.wilsens@maastrichtuniversity.nl.
*E-mail laurence.hawke@maastrichtuniversity.nl.
ORCID
Carolus H. R. M. Wilsens: 0000-0003-3063-9510
Gerrit W. M. Peters: 0000-0001-7208-5128
Sanjay Rastogi: 0000-0002-7804-7349
Notes
The authors declare no competing financial interest.

ACKNOWLEDGMENTS

REFERENCES

(1) Lotz, B.; Miyoshi, T.; Cheng, S. Z. C. 50th Anniversary Perspective: Polymer Crystals and Crystallization: Personal Journeys in a Challenging Research Field. *Macromolecules* **2017**, *50*, 5995−6025.
(2) Beck, H. N. Heterogeneous nucleating agents for polypropylene crystallization. *J. Appl. Polym. Sci.* **1967**, *11*, 673.
(3) Phillips, A. W.; Bhatia, A.; Zhu, P.-W.; Edward, G. Shish Formation and Relaxation in Sheared Isotactic Polypropylene Containing Nucleating Particles. *Macromolecules* **2011**, *44*, 3517−3528.
(4) Somani, R. H.; Yang, L.; Hsiao, B. S.; Agarwal, P. K.; Fruitwala, H. A.; Tsou, A. H. Shear-Induced Precursor Structures in Isotactic Polypropylene Melt by in-Situ Rheo-SAXS and Rheo-WAXD Studies. *Macromolecules* **2002**, *35*, 9096−9104.
(5) Li, L. B.; de Jeu, W. H. Shear-Induced Crystallization of Poly(butylene terephthalate): A Real-Time Small-Angle X-ray Scattering Study. *Macromolecules* **2004**, *37*, 5646−5652.

(6) Kumaraswamy, F.; Issaian, A. M.; Kornfield, J. A. Shear-Enhanced Crystallization in Isotactic Polypropylene. 1. Correspondence between in Situ Rheo-Optics and ex Situ Structure Determination. *Macromolecules* **1999**, *32*, 7537−7547.

(7) Wang, J.; Wang, X.; Wang, Q.; Xu, C.; Wang, Z. Effect of Flowing Preformed Spherulites on Shear-Induced Melt Crystallization Behaviors of Isotactic Polypropylene. *Macromolecules* **2018**, *51*, 1756−1768.

(8) Yalcin, B.; Valladares, D.; Cakmak, M. Amplification effect of platelet type nanoparticles on the orientation behavior of injection molded nylon 6 composites. *Polymer* **2003**, *44*, 6913−6925.

(9) Jain, S.; Goossens, J. P. G.; Peters, G. W. M.; van Duin, M.; Lemstra, P. J. Strong decrease in viscosity of nanoparticle-filled polymer melts through selective adsorption. *Soft Matter* **2008**, *4*, 1848−1854.

(10) Deshmukh, Y. S.; Wilsens, C. H. R. M.; Leoné, N.; Portale, G.; Harings, J. A. W.; Rastogi, S. Melt-Miscible Oxalamide Based Nucleating Agent and Their Nucleation Efficiency in Isotactic Polypropylene. *Ind. Eng. Chem. Res.* **2016**, *55*, 11756−11766.

(11) Blomenhofer, M.; Ganzleben, S.; Hanft, D.; Schmidt, H.-W.; Kristiansen, M.; Smith, P.; Stoll, K.; Mäder, D.; Hoffmann, K. Designer" Nucleating Agents for Polypropylene. *Macromolecules* **2005**, *38*, 3688.

(12) Varga, J.; Menyhárd, A. Effect of solubility and nucleating duality of N,N′-dicyclohexyl-2,6-naphthalenedicarboxamide on the supermolecular structure of isotactic polypropylene. *Macromolecules* **2007**, *40*, 2422.

(13) Shi, Y.; Xin, Z. Study on variable nucleation efficiency of N,N′-Dicyclohexyl-2,6-naphthalenedicarboxamide on isotactic polypropylene. *J. Thermoplast. Compos. Mater.* **2016**, *29*, 1667.

(14) Ma, P.; Xu, Y.; Wang, D.; Dong, W.; Chen, W. Rapid Crystallization of Poly(lactic acid) by Using Tailor-Made Oxalamide Derivatives as Novel Soluble-Type Nucleating Agents. *Ind. Eng. Chem. Res.* **2014**, *53*, 12888.

(15) Shen, T.; Xu, Y.; Cai, X.; Ma, P.; Dong, W.; Chen, M. Enhanced crystallization kinetics of poly(lactide) with oxalamide compounds as nucleators: effect of spacer length between the oxalamide moieties. *RSC Adv.* **2016**, *6*, 48365.

(16) Ma, P.; Deshmukh, Y. S.; Wilsens, C. H. R. M.; Hansen, M. R.; Graf, R.; Rastogi, S. Self-assembling process of Oxalamide compounds and their nucleation efficiency in bio-degradable Poly-(hydroxyalkanoate)s. *Sci. Rep.* **2015**, *5*, 13280.

(17) Deshmukh, Y. S.; Ma, P.; Wilsens, C. H. R. M.; Rastogi, S. Nucleating agents for biopolymers. WO 2013120793A1, 2013.

(18) Yang, Y.; Liang, R.; Chen, Y.; Zhang, C.; Zhang, R.; Wang, X.; Kong, R.; Chen, Q. Using a Self-Assemblable Nucleating Agent To Tailor Crystallization Behavior, Crystal Morphology, Polymorphic Crystalline Structure, and Biodegradability of Poly(1,4-butylene adipate). *Ind. Eng. Chem. Res.* **2017**, *56* (28), 7910−7919.

(19) Xu, P.; Feng, Y.; Ma, P.; Chen, Y.; Dong, W.; Chen, M. Crystallization behaviours of bacterially synthesized poly-(hydroxyalkanoate)s in the presence of oxalamide compounds with different configuration. *Int. J. Biol. Macromol.* **2017**, *104*, 624−630.

(20) Xing, Q.; Li, R.; Dong, X.; Luo, F.; Kuang, X.; Wang, D.; Zhang, L. Enhanced Crystallization Rate of Poly(L -lactide) Mediated by a Hydrazide Compound: Nucleating Mechanism Study. *Macromol. Chem. Phys.* **2015**, *216* (10), 1134−1145.

(21) Marco, C.; Ellis, G.; Gómez, M. A.; Arribas, J. M. Comparative study of the nucleation activity of third-generation sorbitol-based nucleating agents for isotactic polypropylene. *J. Appl. Polym. Sci.* **2002**, *84*, 2440.

(22) Balzano, L.; Portale, G.; Peters, G. W. M.; Rastogi, S. Thermoreversible DMDBS Phase Separation in *i*PP: The Effects of Flow on the Morphology. *Macromolecules* **2008**, *41*, 5350.

(23) Wilsens, C. H. R. M.; Hawke, L. G. D.; Troisi, E. M.; Hermida-Merino, D.; de Kort, G.; Leoné, N.; Saralidze, K.; Peters, G. W. M.; Rastogi, S. Effect of Self-Assembly of Oxalamide Based Organic Compounds on Melt Behavior, Nucleation, and Crystallization of Isotactic Polypropylene. *Macromolecules* **2018**, *51* (13), 4882−4895.

(24) Xu, J.-Z.; Chen, C.; Wang, Y.; Tang, H.; Li, Z.-M.; Hsiao, B. S. Graphene Nanosheets and Shear Flow Induced Crystallization in Isotactic Polypropylene Nanocomposites. *Macromolecules* **2011**, *44*, 2808−2818.

(25) Nam, Y.; Shim, K. B.; Kim, S. H.; Kim, B. C. Effect of Silica Nanoparticle on the Quiescent and the Shear Induced Crystallization Behaviors of Poly(trimethylene terephthalate). *Polym. J.* **2004**, *36* (7), 519−530.

(26) D'Haese, M.; van Puyvelde, P.; Langouche, F. Effect of Particles on the Flow-Induced Crystallization of Polypropylene at Processing Speeds. *Macromolecules* **2010**, *43*, 2933−294.

(27) D'Haese, M.; Langouche, F.; van Puyvelde, P. On the Effect of Particle Size, Shape, Concentration, and Aggregation on the Flow-Induced Crystallization of Polymers. *Macromolecules* **2013**, *46*, 3425−3434.

(28) Patil, N.; Balzano, L.; Portale, G.; Rastogi, S. A Study on the Chain-Particle Interaction and Aspect Ratio of Nanoparticles on Structure Development of a Linear Polymer. *Macromolecules* **2010**, *43*, 6749−6759.

(29) Zhang, Q. D.; Lippits, D.; Rastogi, S. Dispersion and rheological aspects of SWNTs in intractable polymers. *Macromolecules* **2006**, *39* (2), 658−666.

(30) van Erp, T. B.; Balzano, L.; Spoelstra, A. B.; Govaert, L. E.; Peters, G. W. M. Quantification of non-isothermal, multi-phase crystallization of isotactic polypropylene: The influence of shear and pressure. *Polymer* **2012**, *53*, 5896−5908.

(31) Bras, W.; Dolbnya, I. P.; Detollenaere, D.; van Tol, R.; Malfois, M.; Greaves, G. N.; Ryan, A. J.; Heeley, E. Recent experiments on a small-angle/wide-angle X-ray scattering beam line at the ESRF. *J. Appl. Crystallogr.* **2003**, *36*, 791.

(32) Portale, G.; Cavallo, D.; Alfonso, C.; Hermida-Merino, D.; van Drongelen, M.; Balzano, L.; Peters, G. W. M.; Goossens, J. P. G.; Bras, W. Polymer crystallization studies under processing-relevant conditions at the SAXS/WAXS DUBBLE beamline at the ESRF. *J. Appl. Crystallogr.* **2013**, *46*, 1681.

(33) Troisi, E. M.; Portale, G.; Ma, Z.; van Drongelen, M.; Hermida-Merino, D.; Peters, G. W. M. Unusual Melting Behavior in Flow Induced Crystallization of LLDPE: Effect of Pressure. *Macromolecules* **2015**, *48* (8), 2551−2560.

(34) Housmans, J.-W.; Gahleitner, M.; Peters, G. W. M.; Meijer, H. E. H. Structure−property relations in molded, nucleated isotactic polypropylene. *Polymer* **2009**, *50*, 2304−2319.

(35) van Drongelen, M.; van Erp, T. B.; Peters, G. W. M. Quantification of non-isothermal, multi-phase crystallization of isotactic polypropylene: The influence of cooling rate and pressure. *Polymer* **2012**, *53*, 4758−4769.

(36) Caelers, H. J. M.; Govaert, L. E.; Peters, G. W. M. The prediction of mechanical performance of isotactic polypropylene on the basis of processing conditions. *Polymer* **2016**, *83*, 116−128.

(37) Housmans, J.-W.; Steenbakkers, R. J. A.; Roozemond, P. C.; Peters, G. W. M.; Meijer, H. E. H. Saturation of Pointlike Nuclei and the Transition to Oriented Structures in Flow-Induced Crystallization of Isotactic Polypropylene. *Macromolecules* **2009**, *42*, 5728−5740.

(38) Yoshioka, Y.; Tashiro, K. Structural change in the Brill transition of Nylon m/n (1) Nylon 10/10 and its model compounds. *Polymer* **2003**, *44*, 7007−7019.

(39) Yoshioka, Y.; Tashiro, K.; Ramesh, C. Structural change in the Brill transition of Nylon m = n (2) conformational disordering as viewed from the temperature-dependent infrared spectral measurements. *Polymer* **2003**, *44*, 6407−6417.

(40) Ianniruberto, G. Extensional Flows of Solutions of Entangled Polymers Confirm Reduction of Friction Coefficient. *Macromolecules* **2015**, *48*, 6306−6312.

(41) Münstedt, H.; Köppl, T.; Triebel, C. Viscous and elastic properties of poly(methyl methacrylate) melts filled with silica nanoparticles. *Polymer* **2010**, *51*, 185−191.

(42) Ballard, D. G. H.; Cheshire, P.; Longman, G. W.; Schelten, J. Small-angle neutron scattering studies of isotropic polypropylene. *Polymer* **1978**, *19*, 379.

(43) Yezek, L.; Schärtl, W.; Chen, Y.; Gohr, Y.; Schmidt, M. Influence of Hair Density and Hair Length on Interparticle Interactions of Spherical Polymer Brushes in a Homopolymer Matrix. *Macromolecules* **2003**, *36*, 4226−4235.

(44) Castaing, J.-C.; Allain, C.; Auroy, P.; Auvray, L. Rheology of nanosized hairy grain suspensions. *Eur. Phys. J. B* **1999**, *10*, 61−70.

(45) Akcora, P.; Kumar, S. K.; Moll, J.; Lewis, S.; Schadler, L. S.; Li, Y.; Benicewicz, B. W.; Sandy, A.; Narayanan, S.; Ilavsky, J.; Thiyagarajan, P.; Colby, R. H.; Douglas, J. F. Gel-like" Mechanical Reinforcement in Polymer Nanocomposite Melts. *Macromolecules* **2010**, *43*, 1003−1010.

(46) Milner, S. T.; McLeish, T. C. B. Parameter-free theory for stress relaxation in star polymer melts. *Macromolecules* **1997**, *30*, 2159−2166.

(47) Das, C.; Inkson, N. J.; Read, D. J.; Kelmanson, M. A.; McLeish, T. C. B. Computational linear rheology of general branch-on-branch polymers. *J. Rheol.* **2006**, *50* (2), 207−234.

(48) Yuryev, Y.; Wood-Adams, P. Rheological properties of crystallizing polylactide: Detection of induction time and modeling the evolving structure and properties. *J. Polym. Sci., Part B: Polym. Phys.* **2010**, *48*, 812−822.

(49) Hawke, L. G. D.; Ahmadi, M.; Goldansaz, H.; van Ruymbeke, E. Viscoelastic properties of linear associating poly(n-butyl acrylate) chains. *J. Rheol.* **2016**, *60*, 297−310.

(50) Hao, X.; Kaschta, J.; Schubert, D. W. Viscous and elastic properties of polylactide melts filled with silica particles: Effect of particle size and concentration. *Composites, Part B* **2016**, *89*, 44−53.

(51) Ma, Z.; Balzano, L.; Van Erp, T.; Portale, G.; Peters, G. W. M. Short-Term Flow Induced Crystallization in Isotactic Polypropylene: How Short Is Short? *Macromolecules* **2013**, *46*, 9249−9258.

(52) Roozemond, P. C.; van Drongelen, M.; Ma, Z.; Spoelstra, A. B.; Hermida-Merino, D.; Peters, G. W. M. Self-regulation in flow induced structure formation of polypropylene. *Macromol. Rapid Commun.* **2015**, *36*, 385−390.

(53) Kanaya, T.; Polec, I. A.; Fujiwara, T.; Inoue, R.; Nishida, K.; Matsuura, T.; Ogawa, H.; Ohta, N. Precursor of Shish-Kebab above the Melting Temperature by Microbeam X-ray Scattering. *Macromolecules* **2013**, *46*, 3031−3036.

(54) Matsuura, T.; Murakami, M.; Inoue, R.; Nishida, K.; Ogawa, H.; Ohta, N.; Kanaya, T. Microbeam Wide-Angle X-ray Scattering Study on Precursor of Shish Kebab. Effects of Shear Rate and Annealing on Inner Structure. *Macromolecules* **2015**, *48*, 3337−3343.